



ON THE BRIGHT LOOP TOP EMISSION IN POST-ERUPTION ARCADES

ROHIT SHARMA¹, DURGESH TRIPATHI², HIROAKI ISOBE³, AND AVYARTHANA GHOSH^{2,4}¹National Centre for Radio Astrophysics, Post Bag 4, Ganeshkhind, Pune 411007, India²Inter-University Centre for Astronomy and Astrophysics, Post Bag 4, Ganeshkhind, Pune 411007, India³Graduate School of Advanced Integrated Studies in Human Survivability, Kyoto University, 1 Yoshida-Nakaadachi-cho, Sakyo-ku, Kyoto 603-8306, Japan⁴IISER-Kolkata, Mohanpur—741246, West Bengal, India

Received 2016 January 12; accepted 2016 March 15; published 2016 May 20

ABSTRACT

Observations of post-eruption arcades (PEAs) in X-rays and EUV reveal strong localized brightenings at the loop top regions. The origins of these brightenings and their dynamics are not well understood to date. Here, we study the dynamics of PEAs using one-dimensional hydrodynamic modeling, focusing on understanding the formation of localized brightening. Our findings suggest that these brightenings are the result of collisions between the counter-streaming chromospheric evaporation from both the footpoints. We perform forward modeling of the emission observed in simulated results in various spectral lines observed by the Extreme-Ultraviolet Imaging Telescope on board *Hinode*. The forward-modeled intensities in various spectral lines are in close agreement with a flare observed on 2006 December 17 by EIS.

Key words: Sun: flares – Sun: UV radiation

1. INTRODUCTION

Solar flares are possibly the brightest and most energetic bursts that occur in the atmosphere of the Sun. They release a high amount of radiation and energetic particles into the interplanetary medium and play a key role in determining space weather. Our understanding of the physics of solar flares is at a level where there exists a “standard model” in which plasma ejection and magnetic reconnection play key roles (Shibata & Magara 2011); nevertheless, there still remain many physical processes that are poorly understood. One such challenge is explaining the loop top emission observed in EUV and soft X-ray observations of post-flare loops or post-eruption arcades (Priest & Forbes 2002), which are considered to be one of the best proxies for coronal mass ejection (CME) source regions (Tripathi et al. 2004). However, no one-to-one correlation exists (see, e.g., Ma et al. 2010; Howard & Harrison 2013; Chen et al. 2015; Sun et al. 2015).

One of the first observations of loop top emission in soft X-ray images was reported by Acton et al. (1992). Using the data taken from the Soft X-ray Telescope (SXT) (Tsuneta et al. 1991) on board *Yohkoh* for 10 flares, Acton et al. (1992) found the presence of compact X-ray sources at the loop tops, which were underneath the cusp-shape structures (Forbes & Acton 1996). Studying the flare that occurred on 1992 January 13th, using the observations recorded by SXT and hard X-ray telescope (HXT; Kosugi et al. 1991; Tsuneta et al. 1991), Masuda et al. (1994) discovered hard X-ray sources at the loop top as well as the two footpoints of post-flare loops. The HXR loop top observed by Masuda et al. (1994) was located at the top of the SXR cusp detected in the SXT images. The presence of cusp and co-spatial HXR emission were attributed to magnetic reconnection processes (Forbes & Acton 1996; Priest & Forbes 2002). However, there is no consensus on the origin of the soft X-ray and EUV brightening at the loop top.

With the launch of *Hinode*, it became possible to observe flares across a range of temperatures using the X-Ray Telescope (XRT) and the Extreme-ultraviolet Imaging

Spectrometer (EIS). Hara et al. (2008) reported the XRT and EIS observations of a limb flare on 2006 December 17 that show a clear cusp-structure and the loop top brightening. With the EIS instrument, Hara et al. (2008) could investigate the flare dynamics across a range of temperatures. Some iron and calcium spectral lines with formation temperatures from $\log T = 6.0$ to 6.7 are shown in Table 1. In Figure 1, panels (a)–(g) show intensity maps for six iron lines, Fe x to Fe xv, and Ca xvii. In the same figure, the panel (h) shows zoomed-in maps of the loop top region and contours of Fe xv and Fe xii. As seen in Figure 1, panel (h), and Table 1, hotter plasma is located at higher coronal heights (i.e., in the outer loops) and cooler plasma is located at lower coronal heights (in the inner loops). These are the well-known characteristics, established since the *Yohkoh* observations (Tsuneta 1996), that are consistent with the “standard model” with magnetic reconnection (Yokoyama & Shibata 2001). A number of authors have shown that the loop top brightening is not only seen in SXR, but also in EUV observations using the narrowband imager (see, e.g., Golub et al. 1999; Warren et al. 1999; Warren 2000; Warren & Reeves 2001; Warren & Doschek 2006) obtained by the Transition Region and Coronal Explorer (TRACE; Handy et al. 1999). However, Hara et al. (2008), for the first time, made a clear distinction using the spectroscopic observations by *Hinode*/EIS.

There have been numerous attempts to explain the above described phenomenon using various approaches such as hydrodynamic modeling of multiple loops (Hori et al. 1997), one-dimensional (1D) hydrodynamic modeling in soft X-ray and EUV for SXT and TRACE, respectively (Reeves et al. 2007), and retracting loops forming gas-dynamic shock (Longcope et al. 2009; Longcope & Guidoni 2011). However, there is no consensus on the reason behind the observed loop top brightenings in SXR and EUV.

The loop top brightening can be quantified by taking the ratios of the intensities at the loop top region and the arm regions of the coronal loop shown in the green boxes in Figure 1 and is called the brightening factor (β_{obs}). The

Table 1
The Observation Parameters for Various Spectral Lines for the 2006 December 17th Flare

Spectral Lines	Wavelength (in Å)	Peak Formation Temperature (log T)	Loop Top Intensity (erg cm ⁻² s ⁻¹ str ⁻¹)	Brightening Factor (β_{obs})
Fe x	184.54	6.00	5.1×10^3	3.67
Fe xi	188.23	6.08	2.6×10^4	2.32
Fe xii	195.12	6.10	1.2×10^4	2.91
Fe xiii	202.04	6.15	5.7×10^3	1.54
Fe xiv	274.2	6.25	7.6×10^3	1.65
Fe xv	284.16	6.30	6.5×10^4	2.18
Ca xvii	192.82	6.70	6.8×10^3	2.70

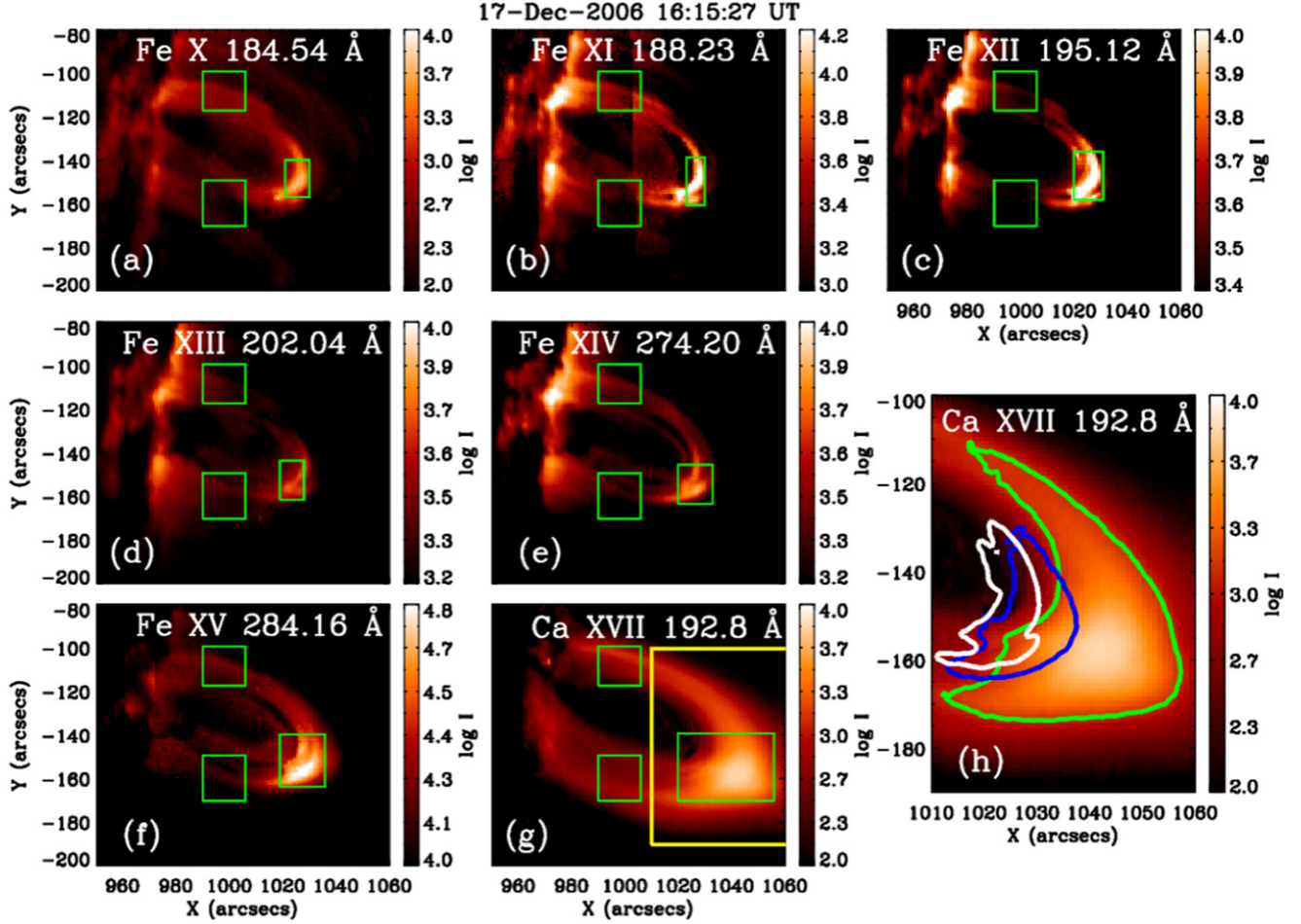


Figure 1. Intensity maps (a)–(g) for various spectral lines shown in Table 1. The green boxes show the area taken for the calculation of the parameter brightening factor. Panel (h) is a zoom-in of the yellow box of the Ca xvii map in panel (g). The intensity contours in panel (h) are Ca xvii (thick green), Fe xv (blue), and Fe xii (white). Note that the contours are at 7% of the level of the maximum intensity in respective lines.

intensity in the arm regions is calculated by averaging over two coronal arm regions (Figure 1). Table 1 shows the intensity values and β_{obs} at the loop top for various spectral lines. β_{obs} varies in the range of 1.5–3.7. Note that the Fe xv is the brightest spectral line.

In order to explain the bright knots observed in EUV post flares loops with various instruments (Cheng et al. 1980; Widing & Hiei 1984; Dere et al. 1997; Golub et al. 1999; Warren 2000), Patsourakos et al. (2004) performed a 1D hydrodynamic modeling, similar to the calculations performed by Antiochos (1980). It was found that the formation of these bright knots can be explained by spatially localized heating that may be occurring during the decay phase of the flares rather than spatially uniform heating.

In this study we take a similar approach to study the evolution of the loop top emission in post-flare loops observed in soft X-ray and EUV observations. We further perform forward modeling and compare our simulation results with observations provided by EIS for the flare that was studied by Hara et al. (2008). The rest of the paper is structured as follows. In Section 2 we provide the details of the numerical model along with initial and boundary conditions. Section 3 summarizes the simulation results. The role of energetics and evolution of density, temperatures, and velocity are discussed for various heating inputs. Section 4 deals with the forward modeling of the loop tops in EIS spectral wavebands. Lastly, Section 5 features our results and conclusions.

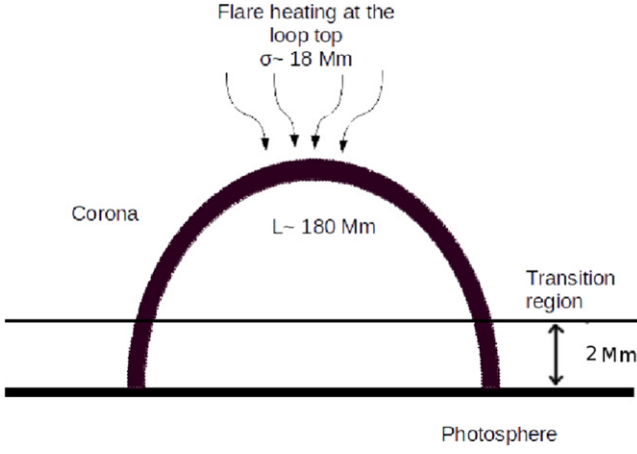


Figure 2. Schematic of the 1D coronal loop, indicating the location of localized flare heating. The total length of the loop (L) is 180 Mm. The transition region location is kept at 2 Mm.

2. NUMERICAL MODEL

We simplify the problem to 1D hydrodynamics of a semi-circular loop with a constant cross-section, as shown in Figure 2. To make the simulation results observationally more viable, we have taken parameters such as the length and the approximate energy deposition, based on the parameters measured for the C-class flare observed on 2006 December 17th, which was studied by Hara et al. (2008). The length of the loop is ~ 180 Mm.

In these simulations we solve the standard hydrodynamic equations, which are described in Equations (1)–(3), with an equation of state of ideal gas in c.g.s. units.

$$\frac{\partial \rho}{\partial t} + \frac{\partial}{\partial s}(\rho v) = 0, \quad (1)$$

$$\frac{\partial}{\partial t}(\rho v) + \frac{\partial}{\partial s}(\rho v^2) = -\rho g_{\parallel} - \frac{\partial P}{\partial s}, \quad (2)$$

$$\frac{\partial E}{\partial t} + \frac{\partial}{\partial s}[(E + P)v] + \rho g_{\parallel} v = \frac{\partial}{\partial s} \left(\kappa_{\parallel} \frac{\partial T}{\partial s} \right) - R + H, \quad (3)$$

where

$$P = nk_B T \quad (4)$$

$$E = \frac{1}{2} \rho v^2 + \frac{P}{\gamma - 1}. \quad (5)$$

Here ρ is the total mass density, v is the fluid velocity, P is the total gas pressure, E is the sum of the kinetic energy and the internal energy per unit volume, T is the plasma temperature, and s is the length along the loop from the left footpoint. We have assumed a monoatomic ideal gas with a specific heat capacity $\gamma = 5/3$. The gravity g_{\parallel} is $g_o \cos\left(\frac{h}{r}\right)$, where h is the height from the photosphere, r is the radius of the curvature of the loop and g_o is $2.7 \times 10^4 \text{ cm s}^{-2}$.

The heat conduction is governed by temperature gradients across the loop, with Spitzer conductivity given by

$$\kappa_{\parallel} = \kappa_0 T^{5/2}, \quad (6)$$

where $\kappa_0 = 9 \times 10^{-7}$. Note that all the units here are in CGS.

In Equation (3) H is a heating function $H(s, t)$ that consists of a static heating H_s and a flare heating term H_f . The functional

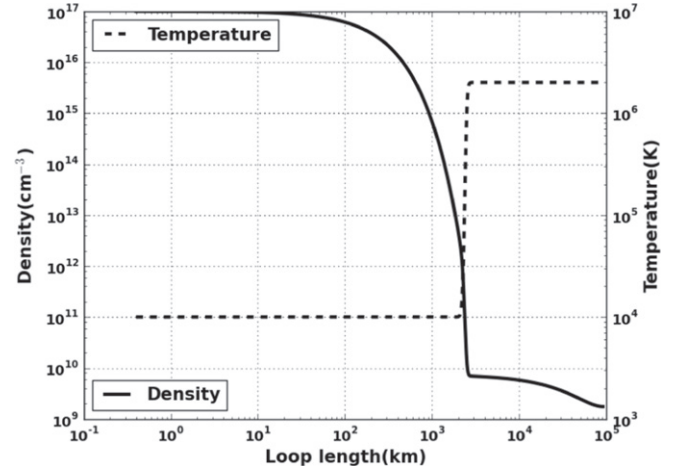


Figure 3. Initial temperature and density profiles for the half loop.

form of H is given as:

$$H(s, t) = H_s(s) + H_f(s, t). \quad (7)$$

The static heating is kept constant to maintain the corona at 2 MK. The flare heating term provides the heating due to the flare, to which the plasma responds and produces the dynamics in the loop. The functional form of the flare heating is given by Equation (8). In this study we have considered the flare heating to have a Gaussian shape with a width of $\sigma \sim 18$ Mm. The mean of the Gaussian is placed at the loop top $s_{\text{top}} \sim 90$ Mm.

$$H_f(s, t) = q(t) \frac{H_o}{\sqrt{2\pi}\sigma} \exp\left(-\frac{(s - s_{\text{top}})^2}{2\sigma^2}\right) (\text{erg cm}^{-2}), \quad (8)$$

where $q(t)$ is the binary switch for the flare heating, i.e., if $q(t)$ is 0 then heating is off, and if it is 1 then heating is on. H_o defines the heating strength, which is kept as a variable. By varying H_o , we can study the dynamics of plasma in flare loops with varying heating strengths.

R in Equation (3) is the radiative cooling, which is defined as

$$R(s, t) = \frac{1}{2} n_e^2 Q(T), \quad (9)$$

where $Q(T)$ is the radiative loss function for optically thin plasma and is approximated through various power-law functions in different temperature bands in the format $Q(T) = \chi T^\alpha (\text{erg s}^{-1} \text{cm}^{-3})$ and taken directly from Hori et al. (1997).

Figure 3 shows the initial conditions for our simulation. We have started the simulations with realistic initial conditions in terms of temperature and density profile for the solar atmosphere. The system is set up in such a way that the loop is in hydrostatic equilibrium, i.e., static heating fully compensates the radiative cooling energy. The initial temperature is kept at 2 MK because we are mostly interested in active region post-flare loops, which are best seen in Fe XII lines forming at 2 MK. The density is then computed along the loop using the equations of hydrostatic equilibrium.

We have also considered the loop to be symmetric across its length. Considering this geometry leads us to solve the equations for only half of the loop (from one footpoint to the loop top). The solution of the other part will then become the mirror image. The boundary conditions are set up so that there are no gradients

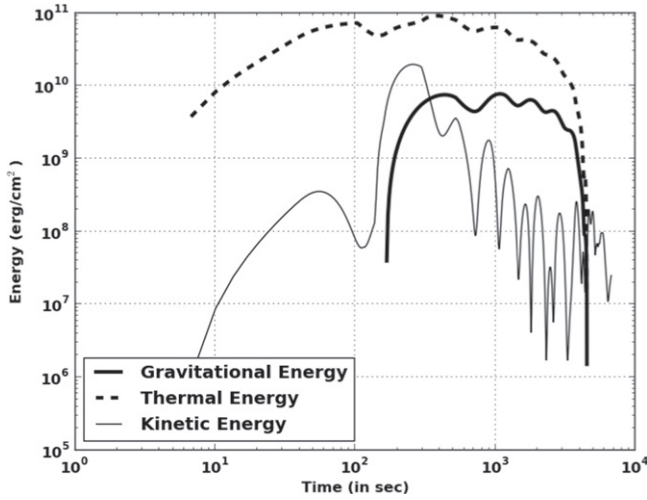


Figure 4. Comparison of the different energies in the corona with time. The gravitational (ΔE_{GE}) and thermal energies (ΔE_{TE}) shown are the variation from the initial gravitational and thermal energies of the loop.

in temperature and density at the loop top. Mathematically the boundary condition can be written as $\left(\frac{\partial n}{\partial s}\right)_{top} = 0$, $\left(\frac{\partial T}{\partial s}\right)_{top} = 0$, and $v_{top} = 0$.

3. RESULTS

3.1. Overview

We have performed simulations for six different external heatings (H_f) applied at the loop top. The heating input to the loop will be 2×10^9 , 2×10^{10} , 4×10^{10} , 8×10^{10} , 1.2×10^{11} , and 2.0×10^{11} erg cm $^{-2}$, uniformly at a time of 100 s each. These energy values correspond to the energy of a C-class flare ($\sim 10^{29}$ erg) distributed over 18 Mm length. We note that the flare observed by Hara et al. (2008) is a C-class flare. A few different values of heating strengths are chosen so as to cover two orders of magnitude centering at C-class flares strengths.

One of the first parameters that needs to be verified is the principle of energy conservation throughout the simulations. We note that before the deposition of any external heat, the system is in hydrostatic equilibrium, i.e., the static heating in the system balances out the radiative cooling. After the heat deposition, we have carefully looked at the different forms of energy available in systems, and their evolutions.

First, we discuss the energetics and dynamics of the loop evolution for the highest heating case, i.e., 2.0×10^{11} erg cm $^{-2}$, in detail. We note that same line of argument will follow for the other heating scenarios. We calculate the total thermal (E_{TE}), kinetic (E_{KE}), and gravitational energy (E_{GE}) in the corona. The coronal part of the loop is defined as the portion of the loop above 2 Mm. Figure 4 shows the temporal evolution of the changes in the total thermal energy (ΔE_{TE}), total kinetic energy (ΔE_{KE}), and total gravitational energy (ΔE_{GE}) in the coronal part of the loop with respect to that at $t = 0$. For an energy component E , $\Delta E = E(t) - E(t = 0)$. There is no total kinetic energy in the loop at $t = 0$, as $v(s) = 0$, so $\Delta E_{KE} = E_{KE}$.

As can be seen from Figure 4, the thermal energy (ΔE_{TE}) starts to increase and attains a maximum at ~ 100 s. This is consistent with fact that the external heat was supplied only for the first 100 s. Thereafter, the thermal energy (ΔE_{TE}) shows

small fluctuations of $\sim 10\%$ and declines sharply after ~ 4000 s. Similarly, kinetic energy (ΔE_{KE}) also increases and attains a maximum at around ~ 60 s. It reaches a minimum at ~ 102 s and rises sharply, reaching a second maximum at ~ 300 s. Thereafter kinetic energy fluctuates and the level of fluctuation in the kinetic energy is $\sim 50\%$. Also, ΔE_{GE} is nil for first 100 s. It starts to increase sharply at ~ 105 s and attains a maximum at 300 s and later fluctuates at $\sim 10\%$ level. Afterward, it falls sharply at around ~ 3500 s.

Figure 5 plots the time evolution of density (panel (a)), temperature (panel (b)), velocity (panel (c)), and pressure (panel (d)). Note that the plots display the above said parameters only for half of the loop. The initial profile for all parameters is plotted at $t = 0$. At $t = 40$ s, the temperature (Figure 5, panel (b)) of the loop top rises to 10 MK and temperature profiles develop a spatially broader profile. The velocity profile (Figure 5, panel (c)) is roughly uniformly negative in higher corona from 25 to 80 Mm, and shows a small bump near ~ 8 Mm.

At $t = 132$ s, the coronal temperature profile flattens to ~ 10 MK. The velocity profile develops a strong positive profile reaching speeds of 200 km s $^{-1}$. The density develops a steep gradient near 20 Mm and the pressure profile now shows a negative dip near the same location. Since the flare heating stops at $t = 100$ s, the coronal temperature dips ($t = 306$ s, panel (b)). At 306 s, the density and pressure profiles (Figure 5, panel (a) and (d)) show a sharp increase at the loop top and velocity (panel (c)) has a large positive profile near the loop top at ~ 88 Mm. The sharp enhancement in density propagates toward the bottom of the loop (Figure 5, panels (a) and (d), $t = 476$ s) with a velocity (panel (c), $t = 476$ s) of 120 km s $^{-1}$. At very large times, $t = 2040$ s, the loop cools down to a few million K. However, the density and pressure profiles quiet and settle. The velocity profile becomes spatially flatter and negative.

The evolution of energy shown in Figure 4, as well as the other physical parameters shown in Figure 5, can be described as follows. As can be seen in Figure 5 panel (b), the external heat input increases the temperature (broader bump at $t = 40$ s), which in turn increases the thermal energy that is reflected in Figure 4 (dashed line). The increase in thermal energy (ΔE_{TE}) creates a pressure gradient from the loop top to the loop bottom (see panel (d), $t = 40$ s) that invokes a downward velocity flow or conduction front (from loop top to loop footpoint) with a speed of 42 km s $^{-1}$ uniformly throughout the corona, as shown in panel (c) ($t = 40$ s). Here, we describe negative velocity as the flow from top to bottom. Due to the downflowing plasma, the kinetic energy (ΔE_{KE}) in the system increases, which is also reflected in Figure 4 (thin solid line).

The downward conduction front (downflow) produced due to the pressure gradient hits the chromosphere at ~ 120 – 130 s and produces fast upflows (see Figure 5 panel (c) $t = 132$ s), a phenomena known as “chromospheric evaporation.” Due to the chromospheric evaporation, the thermal energy (ΔE_{TE}) and kinetic energy (ΔE_{KE}), as well as the gravitational energy (ΔE_{GE}), show an increase. The velocity of the chromospheric evaporation reaches up to ~ 220 km s $^{-1}$. Since the loop is considered to be symmetric and external heat input is at the center of the loop, the evaporation flow has the same speed from both the footpoints. The evaporation flows from the two points collide at the loop top. We refer to it as the primary collision of the evaporation flow and it leads to a sharp increase in density at the loop top (see Figure 5(a) $t = 306$ s), as well as

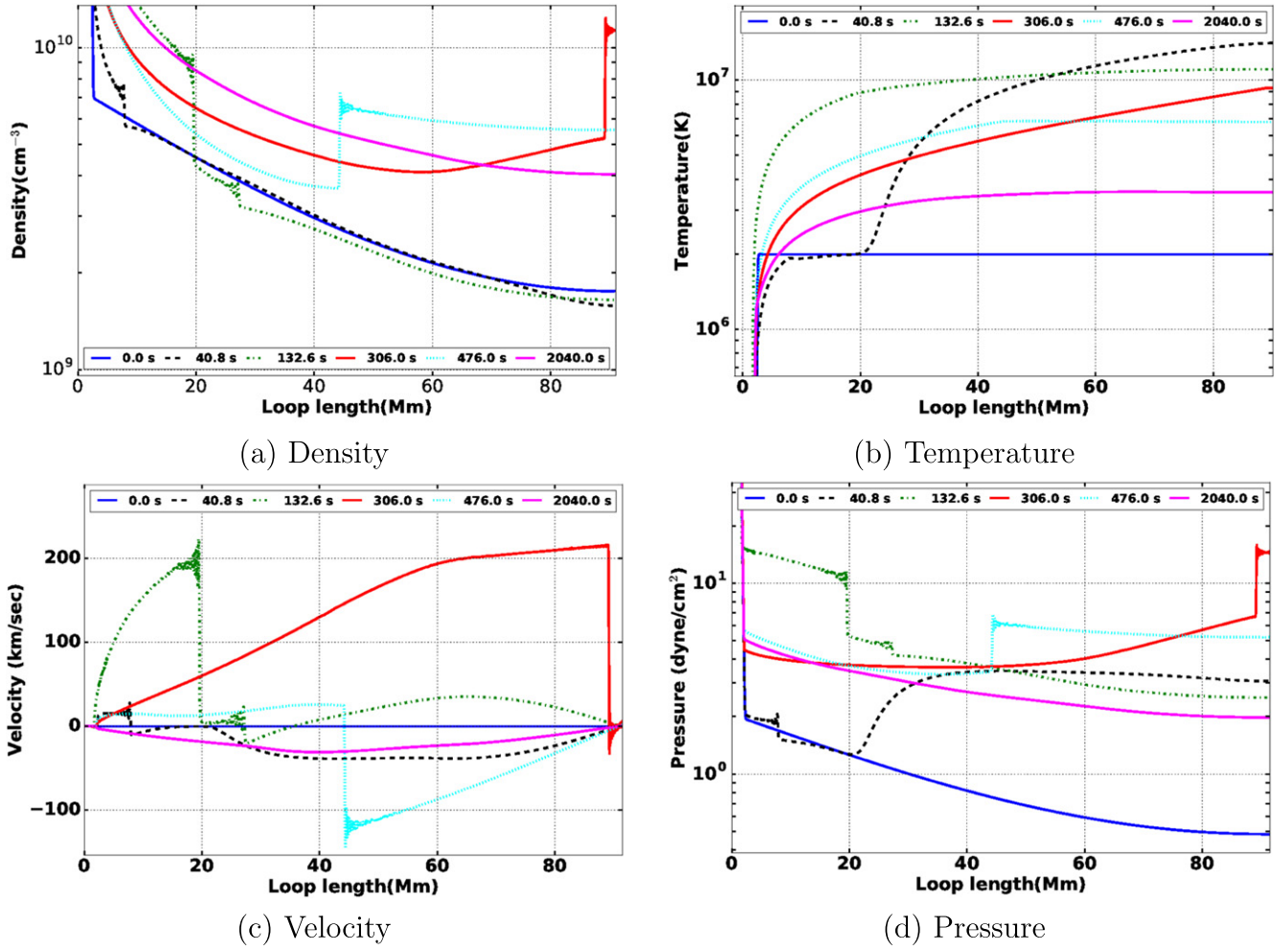


Figure 5. Plots of density, temperature, velocity, and pressure at various times for an input heating of $2 \times 10^{10} \text{ erg cm}^{-2}$.

thermal energy (see Figure 4 dashed line). After the primary collision, the mean kinetic energy (ΔE_{KE}) starts to decline and shows oscillatory behavior. This is indicative of the fact that there may be secondary, tertiary, multiple downflows and upflows. The gravitational energy (ΔE_{GE}), however, remains rather constant until $t = 3500 \text{ s}$, suggesting no significant movement of matter. Therefore, it is plausible to conclude that the secondary and other downflows/upflows replicated in the kinetic energy curve in Figure 4 are weak.

At later times ($\sim 2000 \text{ s}$ and afterward), the density in the corona of the loop is uniformly higher compared to the initial density profile by a factor of 3. The gravitational energy (ΔE_{GE}) remains flat until 2000 s with very small variation (see Figure 4). Both the thermal energy (ΔE_{TE}), as well as the gravitational energy (ΔE_{GE}), show a steep decline afterward. This is indicative of strong cooling and draining of plasma from the corona to the chromosphere.

3.2. Dynamics of the Loop for Various Input Heats

The time evolution of density and temperature along the loop for different heating strengths is shown in Figures 6 and 7. The time steps shown are chosen so as to describe the collision of primary evaporation at the loop top. The strength of the externally supplied heat is given in the figure. As can be clearly seen in the density plots of Figures 6 and 7, the primary flow

collision creates an enhancement in density at the loop top. With the increasing strength of the external heat, the enhancement in density increases and starts to appear at earlier times. The temperature profile of the corona increases uniformly for large heating inputs. To make a quantitative assessment in the changes in density and temperature with increasing heat input, we have defined a parameter “density increment factor” (δ) as the ratio of the loop top density after the collision to the ambient coronal density. The variation of δ and loop top temperature with increasing external heat input is given in Table 2. The table clearly reveals that the density increment factor δ , as well as the loop top temperature, increase as the strength of the external heat input increases. We also calculate the Mach number very close to the loop top just after the collision. For all heating strengths the primary collision remains subsonic.

The increase in density and temperature at loop tops with increasing external heat input can be explained as follows. The stronger heat input creates stronger conduction front from the loop top toward the footpoint and dumps larger matter and energy in the chromosphere. This leads to a stronger evaporation flow. In all the cases, the coronal temperature increases until the first 100 s , corresponding to the heat input time, and then drops as the loop cools. Later on, the coronal part of the loop near the loop top shows an enhancement in the temperature, which corresponds to the time of the primary

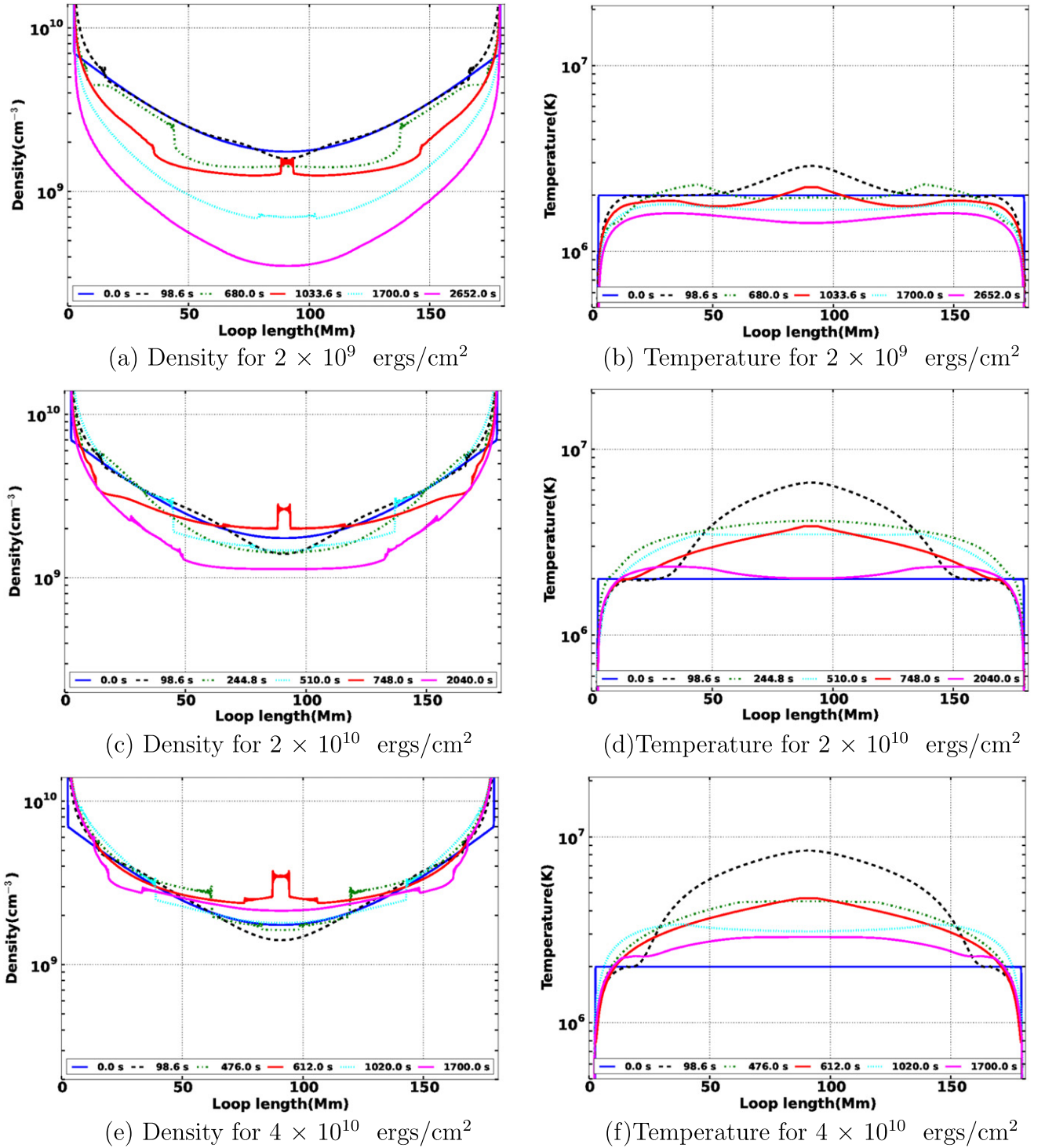


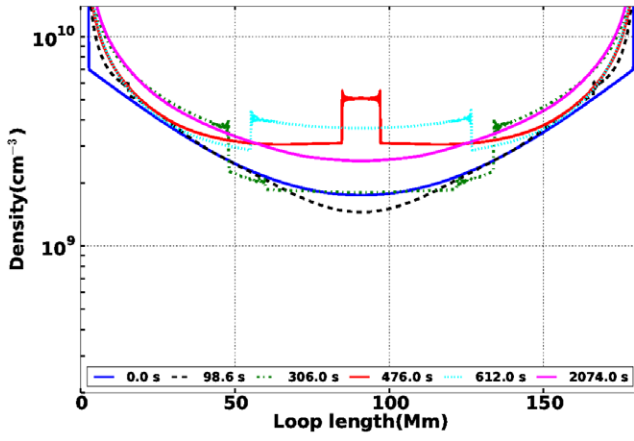
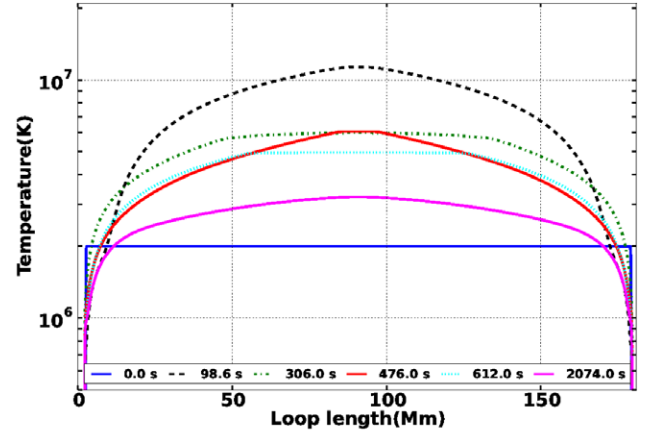
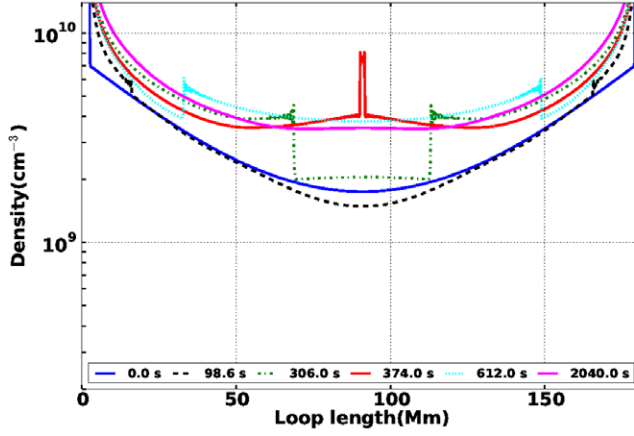
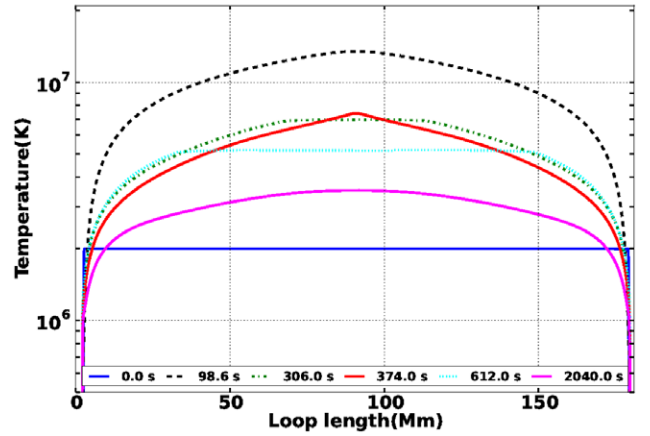
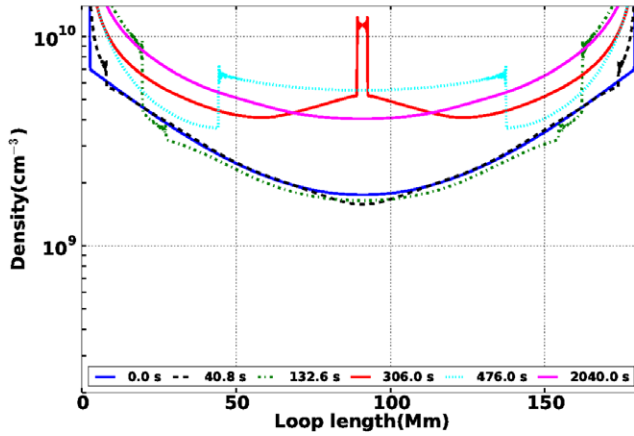
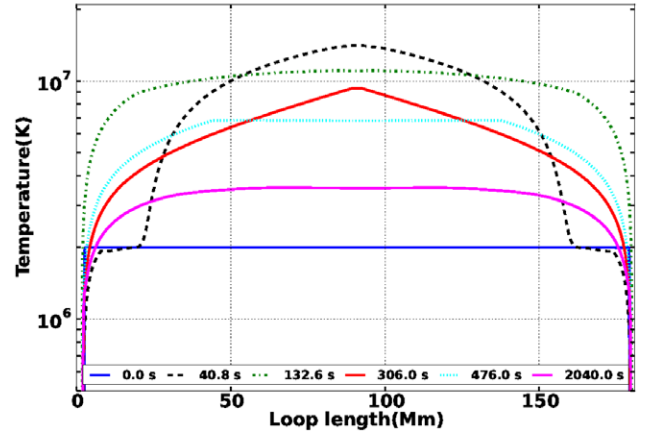
Figure 6. Density and temperature evolution for various heating strengths.

collision of the evaporation flow. This temperature enhancement is strongly related to enhancement in the density (see Figures 6 and 7). After the collision of the primary chromospheric evaporation flow, a reverse flow is created that moves toward the chromosphere and collides with secondary and tertiary flows coming from the chromospheric regions to the coronal region. These flow collisions occur at various places in the loop depending on the flow speeds. However, these collisions are weak and the temperature and density increase is less compared to the primary collision at the loop top. We

expect subsequent reverse flow collisions to be strong for asymmetric heating cases. It may explain the observation of knots seen in EUV observations and modeled by Patsourakos et al. (2004).

4. FORWARD MODELING OF SPECTRAL LINES OBSERVED WITH EIS

The enhancement in the loop top density and temperature is expected to be reflected in various coronal emission lines. In

(a) Density for 8×10^{10} ergs/cm²(b) Temperature for 8×10^{10} ergs/cm²(c) Density for 1.2×10^{11} ergs/cm²(d) Temperature for 1.2×10^{11} ergs/cm²(e) Density for 2×10^{11} ergs/cm²(f) Temperature for 2×10^{11} ergs/cm²**Figure 7.** Density and temperature evolution for various heating strengths.

this section, we forward-model various spectral lines observed by EIS, covering a range of peak formation temperatures of 1.0–5.6 MK. The spectral lines that are forward-modeled and their peak formation temperature are given in Table 3. The peak formation temperature and other atomic parameters are obtained from CHIANTI v.7.0 (Dere et al. 1997; Landi et al. 2013).

The intensity of an optical thin emission line can be written as

$$I_{ij}(\nu) = \int G_{ji}(T_e, n_e) n_e^2 dl, \quad (10)$$

where i and j are upper and lower levels, respectively. $G(T_e, n_e)$ is the contribution function of the spectral line that accounts for

Table 2

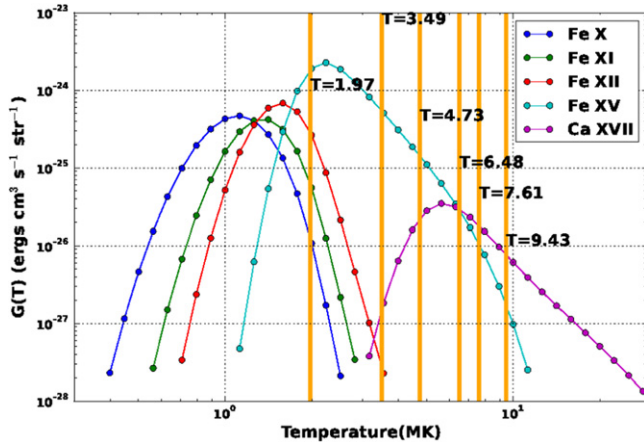
Loop Top Parameters at the Time of Primary Shock Collision for Various Heating Strengths

$H_f \times 10^9$ (erg cm ⁻²)	Factor of Incre- ment (δ)	Coronal Density ($\times 10^8$ cm ⁻³)	T_{top} (MK)	M_a
2.0	1.21	1.52	1.97	0.24
20.0	1.35	2.32	3.49	0.33
40.0	1.36	2.48	4.73	0.39
80.0	1.69	3.98	6.48	0.60
120.0	1.86	4.15	7.61	0.63
200.0	2.17	4.32	9.43	0.62

Note. The Mach number is calculated adjacent to the loop top.**Table 3**

The EIS Spectral Lines Chosen for Forward Modeling

Ionized State	Wavelength (Å)	Peak Formation Temperature (MK)
Fe x	184.54	1.1
Fe xi	188.23	1.4
Fe xii	195.19	1.6
Fe xv	284.16	2.2
Ca xvii	192.8	5.6

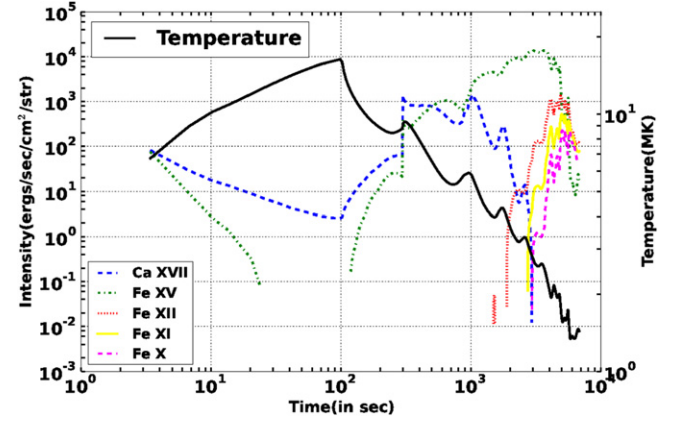
**Figure 8.** Contribution function of the spectral lines listed in Table 3 computed using a density of 10^9 cm⁻³ and coronal abundances of Feldman (1992) and CHIANTI. The orange lines correspond to the loop top temperature (in MK) at the time of the collision of primary flows corresponding to the six simulations with varying heart strength. The temperature increased from $T = 1.97$ MK to $T = 9.43$ MK, corresponding to increasing heating strength.

the ionization fraction and coronal abundances (A_X). It has strong dependence on the electron temperature. The expression for $G(T_e, n_e)$ is given by

$$G_{ji}(T, n_e) = \frac{hc}{4\pi\lambda_{ji}} \frac{A_{ji}}{n_e} \frac{N_j(X^{+k})}{N(X^{+k})} \frac{N(X^{+k})}{N(X)} A_X, \quad (11)$$

where A_{ji} is the spontaneous transition probability for a j to i transition. $\frac{N_j(X^{+k})}{N(X^{+k})}$ is the population of level j relative to the total $N(X^{+k})$ number density of ion X^{+k} . $N(X^{+k})$ and $N(X)$ are the element species in a k th ionized state and neutral state, respectively.

We have computed the contribution function for each spectral line using CHIANTI for a given electron density and the coronal abundances of Feldman (1992). Note that in this

**Figure 9.** Spectral line intensities and temperature of the loop top for an external heating input of 2×10^{11} erg cm⁻². The bold solid line corresponds to the temperature, the dash-dotted line is the intensity of the Fe xv lines, the dashed line is the intensity of the Ca xvii line, the dotted line is the intensity of the Fe xii line, the thin solid line is the intensity of the Fe xi line, and the thick dashed line is the intensity of the Fe x line.

study we are only forward-modeling the spectral lines (given in Table 3), which are not sensitive to density. The contribution functions for all the lines listed in Table 3 are plotted in Figure 8.

We have forward-modeled the loop intensities in all the spectral lines listed in Table 3 using the density and temperatures obtained at each point along the loop. We note that the forward modeling was only performed to the coronal part of the loop. This is essentially due to the fact that the assumption of an optically thin atmosphere will breakdown near the footpoint of the loop in the chromosphere.

Figure 9 displays the evolution of the intensities in these spectral lines at the loop top for the highest heating scenario. In the figure, the bold solid black line corresponds to the temperature at the top, the dash-dotted green line is the intensity of the Fe xv line, the dashed blue line is the intensity of the Ca xvii line, the dotted red line is the intensity of the Fe xii line, the thin solid yellow line is the intensity of the Fe xi line, and the thick dashed magenta line is the intensity of the Fe x line. The temperature at the loop top shows an increase at 100 s, reflecting the time until the external heating was switched on, and decreases afterward.

At initial times ($t \sim 3.4$ s), where the temperature is $T \sim 6.48$ MK, the intensities of Fe xv and Ca xvii are almost the same. As we see from Figure 8, coincidentally, the contribution functions of these two lines cross each other exactly at the temperature $T = 6.48$ MK, which can explain the equal intensity. This temperature nearly corresponds to the peak of the contribution function of Ca xvii and lies on the far right side of that of Fe xv. With an increase in temperature, the intensities in both the spectral lines fall. The emission in Fe xv completely disappears when the temperature reaches roughly 12 MK, as this line has a contribution function, albeit one that is very minimal, reaching a maximum temperature of 10 MK. The intensity in Ca xvii also decreases but never disappears, as the contribution function of this line goes as large as ~ 12 MK.

After 100 s, i.e., when the external heating is switched off, the loop top starts to cool and the intensity in Ca xvii starts to increase, as we move toward the peak of its contribution function. The emission from Fe xv also reappears, albeit later (at $t = 101$ s). At $t = 300$ s, the temperature shows a slight

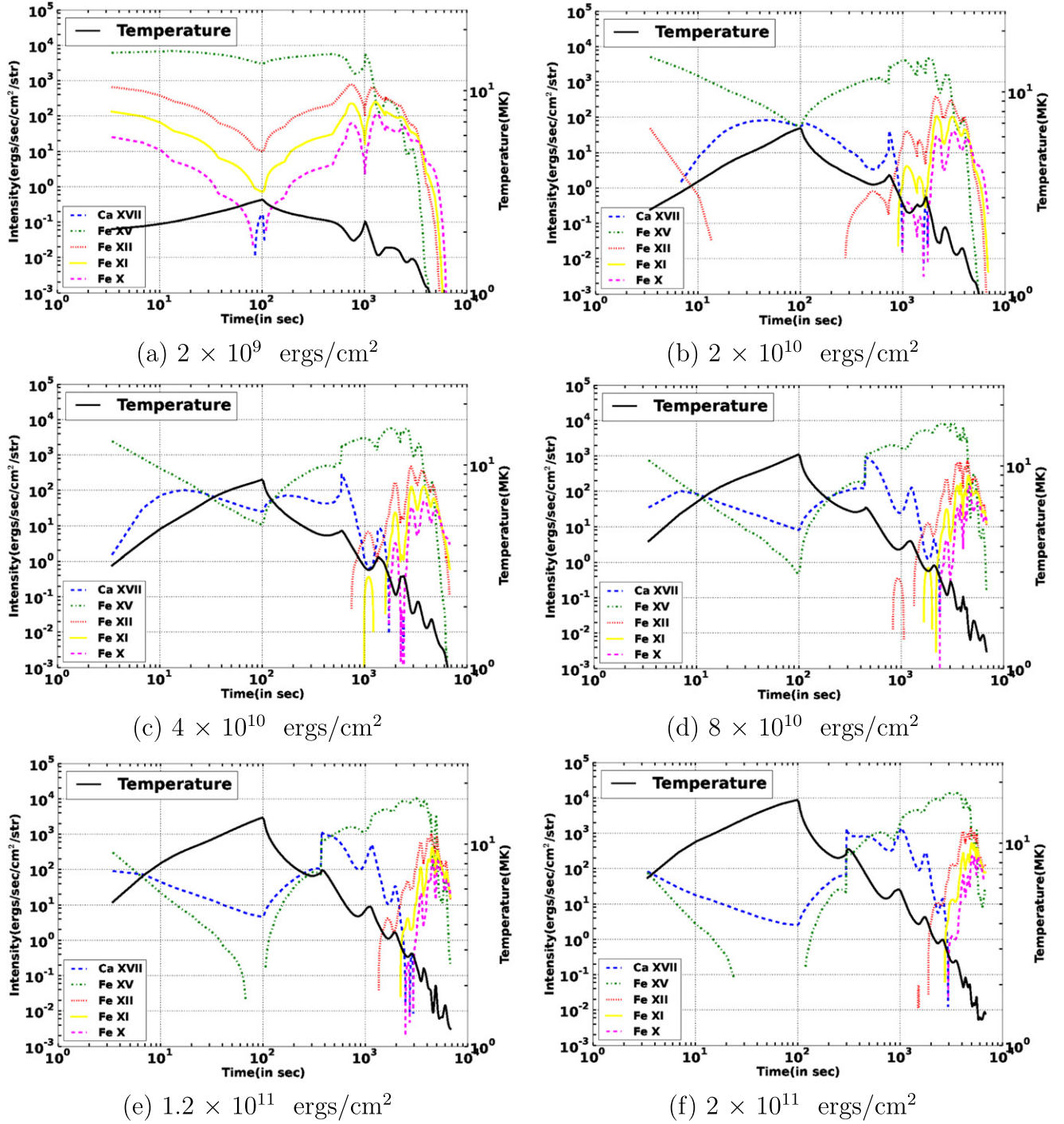


Figure 10. Plots of the intensity variation of the loop top with times for different spectral lines, along with the temperature of the loop top.

enhancement due to the primary collision of the evaporation flow (as explained in Section 3.2 and shown Figure 7). Correspondingly, the intensities in Fe xv and Ca xvii show a slight dip followed by a very sharp increase, which is about two orders of magnitude higher. This sharp enhancement in the intensities coincides with the time of the collision of the primary evaporation flow collision, as well as an enhancement in the density. Later on, the temperature falls and shows many bumps before it dies out. The intensity in Ca xvii remains similar, with some fluctuations until $t=1000$ s, and falls sharply afterward, whereas, the intensity of Fe xv keeps

increasing with oscillations all the way until $t=3000$ s, which corresponds to a temperature of 3 MK. The oscillations in the intensities of Ca xvii, as well as in Fe xv, correspond well with the times of the bumps seen in the temperature profile. These oscillations are essentially due to the collisions of the subsequent evaporation flows. The fall of the intensities of these two lines corresponds to the cool-ward fall of their contribution functions. The spectral lines Fe xii, Fe xi, and Fe x appear at times $t=1040$, 1150 , and 1180 s, respectively, and they do not fade away until the end of the simulation. As the loop cools, the other spectral lines gain in the contribution

Table 4

The Factor of Increment (β_{sim}) in the Modeled EIS Intensities for Various Spectral Lines for Different Heating Strengths along with the Temperature of the Loop Top

$H_f \times 10^9$ (erg cm ⁻²)	Fe x	Fe xi	Fe xii	Fe xv	Ca xvii	T_{top} (MK)
2.0	1.15	1.22	1.30	1.64	2.59	1.97
20.0	1.52	1.55	1.60	1.76	2.12	3.49
40.0	1.67	1.55	1.61	1.76	1.94	4.73
80.0	3.20	2.81	2.77	2.81	2.84	6.48
120.0	3.24	1.64	3.31	3.38	3.42	7.61
200.0	5.06	6.45	2.79	3.83	4.42	9.43

function and this results in an enhancement of their intensities. Also note that the appearance of Fe xii preceded that of Fe x, which can be attributed to their corresponding contribution functions.

After the primary collision ($t = 304$ s), the dips in the temperature correlate with the peaks in the intensities of Fe xv, Fe xii, Fe xi, and Fe x, whereas the reverse is true for Ca xvii as temperature dips correlate with the Ca xvii intensity dips. This is essentially due to the fact that the temperature of the loop top is less than 5.6 MK (peak formation temperature of Ca xvii) and it falls on the positive slope of the contribution function of Ca xvii and the negative slope of that of the Fe xv, Fe xii, Fe xi, and Fe x lines (see Figure 8). If temperature lies on the negative slope in the $G(T)$ curve, any increase in the temperature should show decreases in the intensities of these lines and vice versa. However, we can see in Figures 6 and 7 that the collision of evaporation flows also enhances the densities, which could in turn enhance the emission measure, thereby increasing the intensities. The factor of increase of densities δ for this largest heating case is 2.17, which seen in Table 2.

Figure 10 displays the evolution of intensities at the loop top for different heating strengths. In the figure, the bold black solid line corresponds to the temperature of the top, the dash-dotted green line is the intensity of the Fe xv lines, the dashed blue line is the intensity of the Ca xvii line, the dotted red line is the intensity of the Fe xii line, the thin solid yellow line is the intensity of the Fe xi line, and the thick dashed magenta line is the intensity of the Fe x line. While this explains the evolution of loop top emission in various lines, a similar argument will follow, as is given earlier for the highest heating case. As we can see, the appearance and disappearance of the emission in various spectral lines corresponds well with their respective contribution functions. For example, for the lowest heating case, the emission in Ca xvii appears for a very short duration, only at the time of the peak temperature achieved during heating. Afterward, the emission on Ca xvii dies down. Similarly, the Fe x line appears strongly for the lower heating case at a much earlier time than it appears in the higher heating case (see Figure 10).

We have provided the density increment factor (δ) due to the primary collision of the evaporation flow in Table 2. Corresponding increments in the forward-modeled intensities (β_{sim}) in various spectral lines are given in Table 4. Similar to the definition of the density increment factor, the intensity increment factor (β_{sim}) is also defined as the ratio of intensities at the loop top followed by the primary collision and to the ambient coronal intensity.

The intensity increment factor depends on the temperature of the loop top and the densities. As the density increment factor

(δ) increases with input heat (Table 2), we obtain larger β_{sim} for all spectral lines (Table 4). So in all times, the density becomes most important for increasing the loop top intensity at the time of primary collision. The temperature of the loop top also decides the intensity increment or decrement, as seen in Figure 10, depending on the position of the contribution function (Figure 8).

As can be seen from the table, the loop top temperature can reach up to ~ 10 MK for Ca xvii for the highest heating. It created the maximum intensity increment of about a factor of 4.4 for Ca xvii. The typical β_{sim} is in the range of ~ 1.5 – 3.5 , considering all heating strengths and is close to the brightness factor in observation β_{obs} (Table 1). But among all heating inputs, the 8.0×10^{10} erg cm⁻² input heat case's loop top increment, β_{sim} , shows the closest resemblance to the β_{obs} for all spectral lines, except Fe xi. The case of 1.2×10^{11} erg cm⁻² is closest to Fe xi. Hotter lines produce larger increments of β_{sim} than cooler lines, and it increases as input heat increases. In Table 1, this trend does show up from Fe xiii to Ca xvii. In simulations the Fe xv line (Figure 10, dashed green curve) is dominant for all heating strengths in post-flare times, which is in agreement with the loop top intensity of the observation (Table 1). We note here that there may not be any one-to-one correlation between the observations and forward-modeled results. This could be due to the limitations of the simulations and forward modeling. In the simulations, the dynamics corresponding to one loop strand is being studied, whereas in simulations there will be a collection of strands going through heating and cooling phases simultaneously.

5. SUMMARY AND DISCUSSION

In this paper we have addressed the longstanding problem of localized loop top brightening in post-flare loops observed in soft X-ray and EUV. We performed a 1D hydrodynamic simulation and forward-modeled the intensities in a few spectral lines (see Table 3) observed by EIS. Our results show that the external heating applied at the loop top produces evaporation flows from chromosphere (Figures 6 and 7). These flows collide at the loop top and enhance the density at the top. This can be clearly seen by increasing the intensities in various spectral lines (Figure 10). This idea of density enhancement in coronal loops due to chromospheric evaporation is also supported in recent studies such as Takasao et al. (2015) and the references therein. Moreover, once the heating is switched off, the temperature of the loop top drops sharply due to enhanced radiative cooling. The decline in temperature is larger for stronger heating cases. This is essentially due to the fact that evaporation flows are stronger, bringing more mass in the loops and thereby increasing the density. We find that temperature of the loop top is an important parameter that determines loop top intensity in post-flare times. However, the density increments δ (see Table 2) are also proportional to the strength of the loop top intensities (Table 4). The intensity increments (β_{sim}) at the time of primary collision are close to the observations β_{obs} (Table 1). Our forward modeling shows that Fe xv has the strongest lines for all the heating strengths in the post-flare loops. This is consistent with the observations provided by Hara et al. (2008), as shown in Table 1. In post-flare times, the cooler spectral lines Fe xii, Fe xi, and Fe x appear in decreasing order of their formation temperatures.

Finally, we conclude that the larger the external heating, the stronger the evaporation, therefore creating stronger loop top

brightening in hotter lines. Therefore, the post-flare loops formed in higher energetic flare cases will appear brighter. We know that most of the strong flares are observed from complex magnetic regions, such as, for example, active regions. However, the low-energy flares are often observed from a quiescent part of the Sun's disk. In these cases, a post-flare loop formed due to the flare eruption of subsequent CMEs may not be bright enough to be observed. Further investigations regarding the effects of various parameters such as heating locations, and the geometries of the loops, as well as the length and cross-sections, are required and are under progress. In addition, more observational study is required to provide quantitative constraints on the relative brightening in different spectral lines.

We thank the referee for a careful reading and providing constructive comments. R.S. acknowledges the support of Dr. Divya Oberoi, NCRA-TIFR, Pune. D.T. and A.G. acknowledge the Max-Planck Partner Group of MPS at IUCAA. *Hinode* is a Japanese mission developed and launched by ISAS/JAXA, collaborating with NAOJ as a domestic partner, and NASA and STFC (UK) as international partners. Scientific operation of the *Hinode* mission is conducted by the *Hinode* science team organized at ISAS/JAXA. This team mainly consists of scientists from institutes in the partner countries. Support for the post-launch operation is provided by JAXA and NAOJ (Japan), STFC (UK), NASA, ESA, and NSC (Norway). CHIANTI is a collaborative project involving George Mason University, the University of Michigan (USA), and the University of Cambridge (UK). The authors acknowledge use of CANS (Coordinated Astronomical Numerical Software).

REFERENCES

- Acton, L. W., Feldman, U., Bruner, M. E., et al. 1992, *PASJ*, **44**, L71
 Antichos, S. K. 1980, *ApJ*, **236**, 270
 Chen, H., Zhang, J., Ma, S., et al. 2015, *ApJL*, **808**, L24
 Cheng, C.-C., Tandberg-Hanssen, E., & Smith, J. B., Jr. 1980, *SoPh*, **67**, 259
 Dere, K. P., Landi, E., Mason, H. E., Monsignori Fossi, B. C., & Young, P. R. 1997, *A&AS*, **125**, 149
 Feldman, U. 1992, *PhyS*, **46**, 202
 Forbes, T. G., & Acton, L. W. 1996, *ApJ*, **459**, 330
 Golub, L., Bookbinder, J., Deluca, E., et al. 1999, *PhPl*, **6**, 2205
 Handy, B. N., Acton, L. W., Kankelborg, C. C., et al. 1999, *SoPh*, **187**, 229
 Hara, H., Watanabe, T., Matsuzaki, K., et al. 2008, *PASJ*, **60**, 275
 Hori, K., Yokoyama, T., Kosugi, T., & Shibata, K. 1997, *ApJ*, **489**, 426
 Howard, T. A., & Harrison, R. A. 2013, *SoPh*, **285**, 269
 Kosugi, T., Makishima, K., Murakami, T., et al. 1991, *SoPh*, **136**, 17
 Landi, E., Young, P. R., Dere, K. P., Del Zanna, G., & Mason, H. E. 2013, *ApJ*, **763**, 86
 Longcope, D. W., & Guidoni, S. E. 2011, *ApJ*, **740**, 73
 Longcope, D. W., Guidoni, S. E., & Linton, M. G. 2009, *ApJL*, **690**, L18
 Ma, S., Attrill, G. D. R., Golub, L., & Lin, J. 2010, *ApJ*, **722**, 289
 Masuda, S., Kosugi, T., Hara, H., Tsuneta, S., & Ogawara, Y. 1994, *Natur*, **371**, 495
 Patsourakos, S., Antiochos, S. K., & Klimchuk, J. A. 2004, *ApJ*, **614**, 1022
 Priest, E. R., & Forbes, T. G. 2002, *A&ARv*, **10**, 313
 Reeves, K. K., Warren, H. P., & Forbes, T. G. 2007, *ApJ*, **668**, 1210
 Shibata, K., & Magara, T. 2011, *LRSP*, **8**, 6
 Sun, X., Bobra, M. G., Hoeksema, J. T., et al. 2015, *ApJL*, **804**, L28
 Takasao, S., Matsumoto, T., Nakamura, N., & Shibata, K. 2015, *ApJ*, **805**, 135
 Tripathi, D., Bothmer, V., & Cremades, H. 2004, *A&A*, **422**, 337
 Tsuneta, S. 1996, *ApJ*, **456**, 840
 Tsuneta, S., Acton, L., Bruner, M., et al. 1991, *SoPh*, **136**, 37
 Warren, H., & Doschek, G. 2006, *BAAS*, **38**, 253
 Warren, H. P. 2000, *ApJL*, **536**, L105
 Warren, H. P., Bookbinder, J. A., Forbes, T. G., et al. 1999, *ApJL*, **527**, L121
 Warren, H. P., & Reeves, K. K. 2001, *ApJL*, **554**, L103
 Widing, K., & Hiei, E. 1984, *ApJ*, **281**, 426
 Yokoyama, T., & Shibata, K. 2001, *ApJ*, **549**, 1160